Experimental determination of the temperature-and phase-dependent elastic constants of FeRh

D. Ourdani, Aloïs Castellano, Ashwin Kavilen Vythelingum, Jon Ander Arregi, Vojtěch Uhlíř, Bernard Perrin, M. Belmeguenai, Y. Roussigné, Catherine Gourdon, Matthieu Jean Verstraete, et al.

Experimental determination of the temperature- and phase-dependent elastic constants of FeRh

D. Ourdani,[1,2] A. Castellano,[3] A. K. Vythelingum,[1] J. A. Arregi,[4] V. Uhlíř,[4,5] B. Perrin,[1]
M. Belmeguenai,[2] Y. Roussigné,[2] C. Gourdon,[1] M.J. Verstraete,[3,6] and L. Thevenard[1]

[1]*Sorbonne Université, CNRS, Institut des Nanosciences de Paris, 4 place Jussieu, 75252 Paris, France*
[2]*LSPM, Université Paris 13, Sorbonne Paris Cité, 99 avenue Jean-Baptiste Clément, 93430 Villetaneuse, France*
[3]*NanoMat/Q-Mat Université de Liège, and European Theoretical Spectroscopy Facility, B-4000 Liège, Belgium*
[4]*CEITEC BUT, Brno University of Technology, Purkyňova 123, 612 00 Brno, Czech Republic*
[5]*Institute of Physical Engineering, Brno University of Technology, Technická 2, 616 69 Brno, Czech Republic*
[6]*ITP, Physics Department, Utrecht University 3508 TA Utrecht, The Netherlands*
(*thevenard@insp.jussieu.fr)

(Dated: March 29, 2024)

The elastic constants of an epitaxial film of FeRh have been determined experimentally in both ferromagnetic (FM) and antiferromagnetic (AF) phases, using a combination of Brillouin light scattering and picosecond acoustics experiments. The C_{11} constant is noticeably larger in the FM phase than in the AF phase, while C_{12} and C_{44} are both lower, leading to larger Rayleigh wave velocities in the FM phase than in the AF phase. The elastic constants were calculated numerically using first principles anharmonic modeling and machine-learned interatomic potentials. We find that using a temperature-dependent effective potential is indispensable to correctly reproduce the experimental values to within 80 to 100%. The accurate knowledge of the temperature- and phase-dependencies of the elastic constants of crystalline FeRh are valuable ingredients for the predictive modeling of the acoustic and magneto-acoustic properties of this magnetostrictive material.

INTRODUCTION

FeRh is a fascinating magnetic material discovered in 1938 by M. Fallot [1]. It is currently being revisited in the light of novel magnetic and spintronic applications. Its room-temperature bistable antiferromagnetic (AF) states herald the possibility of robust magnetic encoding [2–5], while its first-order transition to a ferromagnetic (FM) state is responsible for large entropy changes promising solid-state magnetic refrigeration [6, 7]. This transition is accompanied by a substantial ($\sim 1\%$) iso-structural volume change [8, 9] that is intertwined with the magnetic transition [10, 11].

While much attention has been dedicated to the magnetic characteristics of this material, few experimental studies have been devoted to its elastic properties as a function of the magnetic phase and/or temperature. Notably, there is no record of the complete set of elastic constants C_{11}, C_{12} and C_{44} of crystalline cubic FeRh in the literature. The value of C_{11} is the one that is most readily obtained, by measuring the longitudinal acoustic wave velocity and the volume density ρ, with $V_L=\sqrt{\frac{C_{11}}{\rho}}$. Combining this value with a specific heat measurement within a Debye model yields an estimate of the transverse acoustic velocity, and hence C_{44} given that $V_T=\sqrt{\frac{C_{44}}{\rho}}$. This enabled Cooke *et al.* [12] to estimate the values of C_{11} and C_{44} in the AF and FM phases, both obtained at room-temperature by imposing slightly different Rh concentrations in two distinct samples. No value has been provided so far for C_{12}, which is more challenging to measure. There is somewhat more data for *polycrystalline* FeRh [13–15], on which it is straightforward to estimate the Young modulus E by measuring bulk acoustic wave velocities. Finally, there is a substantial corpus of theoretical papers reporting DFT simulations of the phonon band structure of FeRh [16–19], from which the elastic constants in both phases can be estimated. However, to our knowledge, the explicit temperature dependence of the C_{ij} has never been determined.

In this work, we measure experimentally the temperature dependence of C_{11}, C_{12} and C_{44} in both AF and FM phases of the same composition, by a combination of Brillouin Light Scattering (BLS) and picosecond acoustic wave interferometry. We follow the strategy developed for other materials by previous authors [20–23] who measured the dispersion relations of phonons, using either inelastic BLS [20, 21] or time-of-flight methods [23]. For sufficiently complete datasets including different modes (bulk/surface, or Rayleigh/Sezawa), or various crystallographic directions, the elastic constants can be recovered by global fits, e.g. using simplex methods applied to the modeling of the acoustic wave dispersion. Our findings are supported by machine-learning molecular dynamics simulation fits to *ab initio* data, and are in agreement with previously published theoretical estimates [16–19], which report a substantially larger C_{11} and lower C_{12}, C_{44} in the FM phase, with respect to the AF one. Moreover, the measured temperature dependence of the elastic constants is very well corroborated by these temperature-dependent simulations.

The first sections of this article are dedicated to the description of the sample, and the BLS and picosecond acoustics experiments. The following sections describe the analytical modeling of the acoustic dispersion, the resulting deduction of the elastic constants, and a comparison to available theoretical elastic constants from our calculations and the literature.

SAMPLE

The epitaxial 200-nm-thick FeRh film under study was grown on a MgO(001) substrate via DC magnetron sputter-

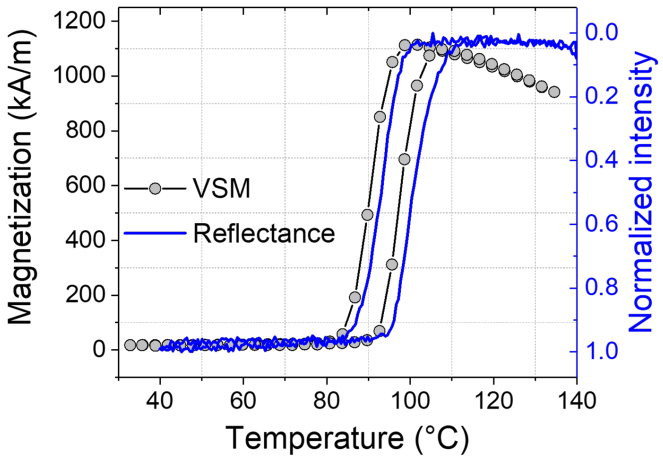

FIG. 1. Characterization of the AF to FM phase transition of FeRh using VSM and reflectivity (inverted scale and normalized to its maximal value).

ing from an equiatomic target. The FeRh film was grown at 430°C after preheating the substrate in high vacuum for 60 min at the same temperature. An Ar pressure of 2.7×10^{-3} mbar and a sputtering power of 50 W led to a deposition rate of 2 nm min^{-1}. The film was then annealed in situ in high vacuum at 780°C for 80 min, and a protective 2-nm-thick Pt capping layer was grown after cooling down the sample below 120°C. X-ray diffraction characterization shows a high-quality FeRh(001) out-of-plane texture of the sample and the attainment of a homogeneous CsCl-type structure, showing cube-on-cube epitaxy with the FeRh unit cell being 45° in-plane rotated with respect to MgO [9]. Strain in the FeRh film is largely relaxed (with the out-of-plane lattice parameter $c = 2.988$ Å approaching the bulk value) due to the relatively large thickness of the film. Transmission electron microscopy imaging of a cross-sectional lamella allowed a more precise determination of the film thickness, $d = 195 \pm 2$ nm [24].

The AF $\leftrightarrow$ FM transition of the sample is characterized by both vibrating sample magnetometry (VSM, probing the entire volume of the sample) and light reflection microscopy (probing the topmost 10 nm of the film into which the λ_R = 635 nm light is absorbed). As shown in Fig. 1, the onset of the transition occurs at very similar temperatures with both methods, respectively $\approx$ 89°C/98°C (warming and cooling branch) from VSM and $\approx$ 94°C/101°C from light reflection. The slight discrepancy in the transition temperatures obtained by these two methods arises from the difference in the probed area and volume. The transition width is relatively narrow ($\approx$ 10°C) and the sample possesses a very low ($\approx$ 16 kA m^{-1}) residual magnetization at room temperature, both confirming the excellent quality of the film.

METHODOLOGY

The experimental approach is the following: using Brillouin Light Scattering, we measure phonon frequencies at fixed temperatures and variable incident wave-vectors to extract the temperature-dependent dispersion relationships of the first three acoustic modes (Rayleigh and two Sezawa modes). We then perform temperature-dependent picosecond acoustic wave interferometry to measure the longitudinal velocity and obtain $C_{11}(T)$. Fixing this value, we then adjust $C_{12}(T)$ and $C_{44}(T)$ to reproduce the BLS-measured dispersion curves. To analyze the anharmonic and elastic properties, we perform first principles calculations for $T = 0$, and then augment these with a machine-learning inter-atomic potential (MLIP) to be able to run large molecular dynamics simulations, and to compute the temperature-dependence of phonons and the corresponding elastic constants.

BRILLOUIN LIGHT SCATTERING MEASUREMENTS

Description of the experiment

Over the past few decades, BLS has proven to be a powerful technique for characterizing elastic (via surface acoustic waves, SAWs) and magnetic (via spin waves, SWs) properties of thin films and multilayer structures. In our BLS experiments, a monochromatic solid-state laser with a wavelength of $\lambda_{BLS} = 532$ nm and a power of 200 mW is focused onto the sample surface after passing through a set of mirrors and lenses. The backscattered beam from the sample (according to elastic and inelastic processes) is directed to a tandem Fabry-Pérot interferometer at (3 + 3)-pass to determine the frequency shift with respect to the incident beam. The wave-vector (k) is determined by the angle of incidence of the laser with respect to the normal to the sample (θ_{in}) according to the relationship: $k = 4\pi \sin\theta_{in}/\lambda_{BLS}$. All the measurements carried out in this work were made for a wave-vector parallel to the [100] (resp. [110]) direction of MgO (resp. FeRh).

In Fig. 2(a) we present three spectra obtained for different k values at room temperature (AF phase). Note that in this phase, magnetic modes are expected to be out of the observed frequency range. Three surface acoustic modes can be seen, corresponding to the Rayleigh and the so-called Sezawa guided waves. Lorentzian fits of these spectra are then performed to obtain the positions of the Stokes (S) and anti-Stokes (aS) lines, which correspond to negative and positive frequency shifts respectively, f_S and f_{aS}. They were found to be identical in absolute value.

Finally, an *in-situ* heating system was integrated into the BLS bench in order to vary the temperature and perform measurements in the uniform AF and FM phases (please refer to Appendix A for technical details). As the temperature was increased to enter the FM phase, a magnetic field of 200 mT was applied to isolate the purely elastic modes.

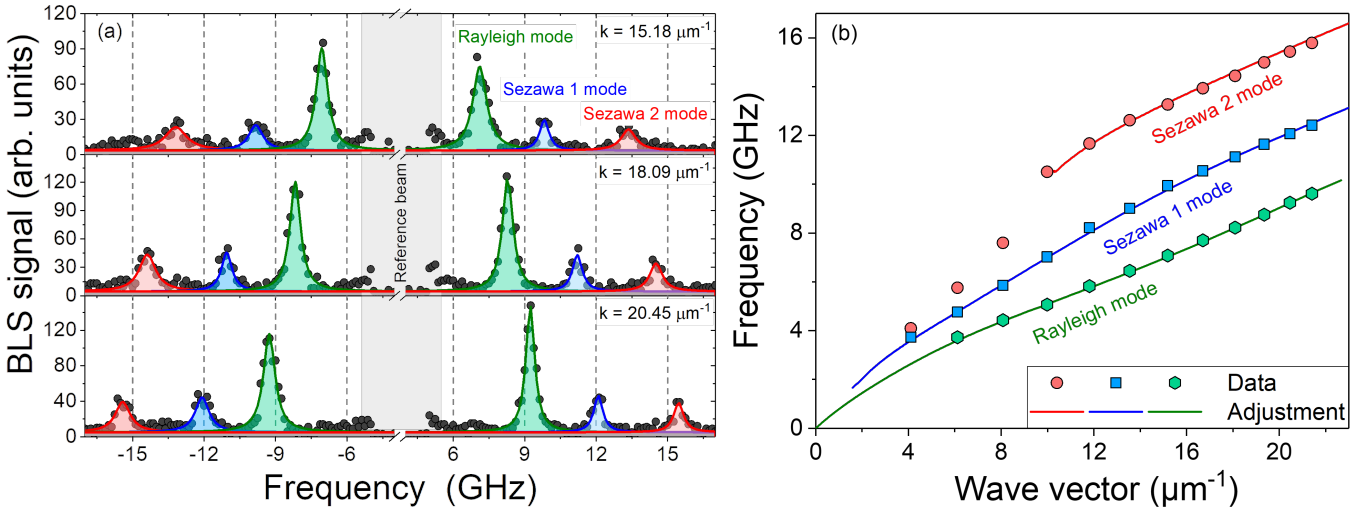

FIG. 2. Room-temperature (T=25°C), antiferromagnetic phase data : (a) BLS spectra at fixed temperature, variable wave-vectors. (b) Dispersion relationship of the first three acoustic surface modes: symbols refer to BLS data and solid lines are calculations with the FeRh elastic coefficients C_{11}=219, C_{12}=148 and C_{44}=125 GPa, optimized via the procedure described in the text.

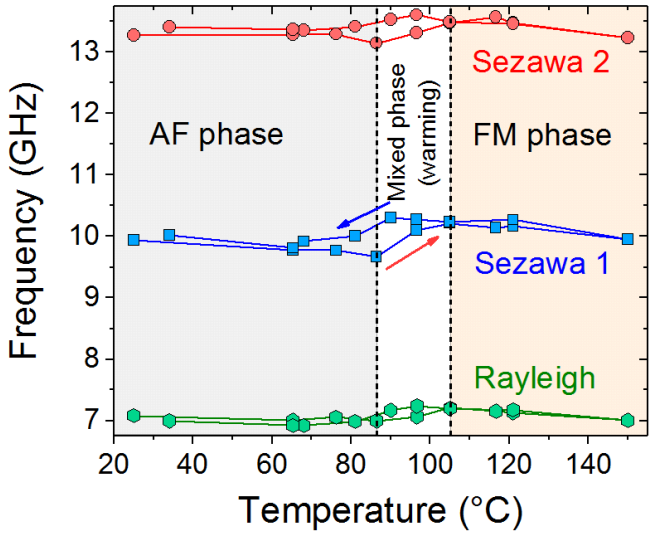

FIG. 3. Acoustic frequencies of the Rayleigh and first two Sezawa modes, measured at k=15.18 μm^{-1} versus temperature. The background color illustrates the nature of the magnetic phase (uniform antiferromagnetic or ferromagnetic, and mixed for the warming branch).

Discussion of $f(T)$ and $f(k)$ curves

Two kinds of spectra were recorded : (i) at a fixed wave-vector and variable temperature (k= 15.18 μm^{-1}) used to locate the phase transition, and (ii) at a fixed temperature and variable wave-vector, giving access to dispersion relationships from which the elastic constants were extracted.

We first comment on the dispersion relationship measurements, performed upon warming, from T=25°C to T=121°C. The measured frequencies reflect the effective acoustic velocities of the entire FeRh film over the MgO substrate system. Because acoustic waves in the magnetic film are *slower* than in the substrate, a dispersive character is obtained, as clearly evidenced in Fig. 2(b) (room temperature measurement). Surface acoustic waves have an evanescent-like decay perpendicular to the surface with a depth of the order of the acoustic wavelength ($2\pi/k$). As the wave-vector increases, the corresponding acoustic wavelength decreases, exploring a volume with a larger fraction of FeRh. At the lowest wave-vector, it is essentially only the MgO substrate that is probed. For the largest probed wave-vector, k=21.4 μm^{-1}, the corresponding phonon wavelength is λ=294 nm, a little thicker than the film.

We now consider how the acoustic frequencies vary during a complete temperature warming/cooling cycle at fixed k = 15.18 μm^{-1} (Fig. 3). Strikingly, by comparing similar temperatures on the warming and cooling branches, one clearly observes a hysteresis opening up, e.g about 0.63 GHz for the first Sezawa mode, 0.46 GHz for the second one and 0.17 GHz for the Rayleigh mode. This behavior is due to the hysteretic nature of the first-order AF↔FM phase transition of FeRh, which can be probed by the acoustic waves given the appreciable ratio λ/d between the wavelength and thickness. The onsets of the transition for the heating and cooling branches occur at approximately the same temperatures as for VSM and reflectivity data in Fig. 1. The slight discrepancy can be attributed to a down-shift of the transition under magnetic field (the −8°C/Tesla shift recorded by Maat *et al.* [25] leads to a −1.6°C shift for the 200 mT field applied here), and to the static heating induced by the CW laser beam. Finally, we emphasize that, away from the transition on either side, all mode frequencies decrease with increasing temperature, a signature of the usual decrease of acoustic velocities upon warming.

PICOSECOND ACOUSTIC MEASUREMENT OF C_{11}

The temperature-dependent BLS measurements give a set of dispersion relations in the AF and FM phases. They reflect the values of the (unknown) FeRh and (known) MgO elastic constants, and the (known) film thickness, and material volume density. In order to narrow the parameter space to determine the C_{ij}s, we measure the longitudinal (bulk) acoustic wave velocity independently.

For this, we use a standard pump-probe technique in which a pump beam impinging on the metallic FeRh surface generates a picosecond-long acoustic pulse [26]. The probe beam is passed through a Sagnac interferometer in order to detect the displacement of the surface. Please refer to Appendix B for more experimental details on this technique.

A typical time delay scan (Fig. 4(a)) results in an electronic peak at the pump-probe coincidence, followed by a slow decay over which appear features (echoes), corresponding to the displacement of the surface upon arrival of the acoustic wave after reflection off the FeRh/MgO interface. We point out that the electronic response is much stronger in the AF phase. While a proper analysis of this interesting feature is out of the scope of this paper, we suggest this might be attributed to the more electrically resistive nature of the low-temperature phase. Within our time window, two echoes are clearly visible, separated in time by a delay Δt related to the longitudinal velocity: $\Delta t = \frac{2d}{V_L}$. Measurements are then performed at discrete rising temperature values on the warming branch of the transition, and the values of $\Delta t(T)$ and $V_L(T)$ are estimated precisely (see Appendix B for details). Using the temperature/phase dependence of the volume density (see Appendix C), we obtain the thermal variations of $C_{11}(T)$ using $V_L(T)=\sqrt{\frac{C_{11}(T)}{\rho(T)}}$ (Fig. 4(b)). The main source of error comes from the ± 2 nm uncertainty on the d=195 nm layer thickness.

As is often the case in solid crystals, C_{11} decreases steadily with temperature. It undergoes a steep jump upon crossing the transition (between T=86°C and 107°C). Despite being minute (a mere 2 ps), the difference in echo delays at the onset of the transition (T=86°C) undoubtedly points to a larger C_{11} constant in the FM phase, with $C_{11,AF} \approx$216-218 GPa between 25°C and 86°C, and $C_{11,FM} \approx$228-232 GPa (T>105°C). These values align with those found by previous authors [12, 13]: Cooke *et al.* had similarly found an increase of C_{11} from 218 to 236 GPa when going from AF to FM by changing the Rh concentration, at T=25°C.

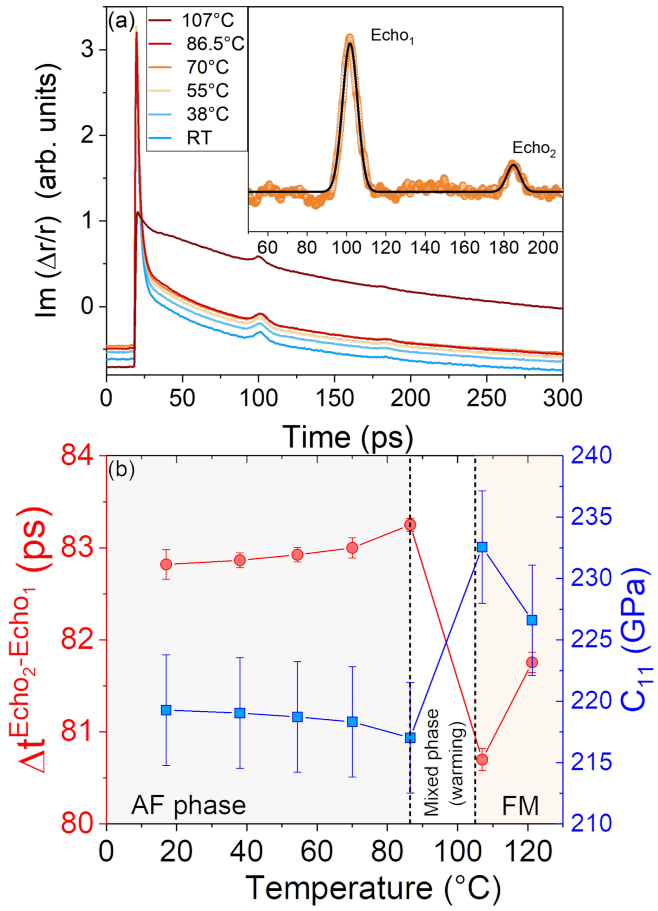

FIG. 4. (a) Longitudinal picosecond acoustic wave interferometry at different temperatures, in the AFM phase up to 86.5°C, and in the FM phase above. Inset: the arrival times of the echoes are found by fitting the data after removal of the thermal background (here T=70°C). See Appendix B for experimental details. (b) The difference in echo arrival time gives the velocity, and from there C_{11} knowing the volume density.

DETERMINATION OF THE ELASTIC CONSTANTS

Fitting procedure

We now follow the "layer-on-substrate" approach of Farnell and Adler [27] to derive the frequency versus wave-vector $f(k)$ relationship of surface acoustic waves propagating along x||[100] (resp. [110]) in MgO (resp. in FeRh). The elastic constants of both materials are expressed in the [100] reference frame of MgO, labelling C^*_{ij} the $\pi/4$-rotated C_{ij} elastic constants of FeRh and $C_{0,ij}$ those of MgO (see Appendix C for the explicit expressions of the $[C]$, $[C^*]$ and $[C_0]$ tensors). Displacement waves in both materials are taken as linear combinations of z-damped terms of the general form $u_i = U_i e^{-\alpha z} e^{j(kx-\omega t)}$ with here i=x,z, $\omega = 2\pi f = Vk$ and $j = \sqrt{-1}$. Injecting these in the elastic dynamical equation and imposing the adequate boundary conditions gives a system of 6 equations, whose determinant $\mathscr{D}(V)$ must be nullified :

$$\mathscr{D}(V) = \begin{vmatrix} 1 & 1 & -1 & -1 & -1 & -1 \\ r_{0,1} & r_{0,2} & -r_1 & -r_2 & -r_3 & -r_4 \\ a_{0,1} & a_{0,2} & -a_1 & -a_2 & -a_3 & -a_4 \\ b_{0,1} & b_{0,2} & -b_1 & -b_2 & -b_3 & -b_4 \\ 0 & 0 & a_1 e^{q_1 kh} & a_2 e^{q_2 kh} & a_3 e^{q_3 kh} & a_4 e^{q_4 kh} \\ 0 & 0 & b_1 e^{q_1 kh} & b_2 e^{q_2 kh} & b_3 e^{q_3 kh} & b_4 e^{q_4 kh} \end{vmatrix} \quad (1)$$

The full procedure is described at length in Appendix C,

as well as the explicit dependency of the coefficients r, a and b on the elastic coefficients of FeRh and V. The roots V_i of Eq. 1 correspond to the different acoustic modes, the lowest one being the Rayleigh wave, the second and third being the first and second Sezawa modes. It is then straightforward to compute $f_i(k) = \frac{V_i k}{2\pi}$ in order to compare to the experimental $f_{exp}(k_{exp})$ of Fig. 2(b).

Inspired by previous work [22, 28], we find the elastic constants of FeRh by testing numerically a large set of (C_{11},C_{12}, C_{44}) values. C_{11} is set by the picosecond acoustics measurements (Fig. 4(b)), while C_{12} was typically searched between 120-200 GPa, and C_{44} between 70-150 GPa in steps of 1 GPa. All the corresponding combinations were tested and we choose the best solution as the triplet that minimizes the following figure of merit χ:

$$\chi = \sum_p \sum_{l_k} |\mathscr{D}(C_{11}, C_{12}, C_{44}, k_{exp,l}, V_p(k_{exp,l})|^2 \qquad (2)$$

In this expression, p=1,2,3 labels the Rayleigh, first and second Sezawa modes, l=1..N_l are the data points for a given mode number, and $V_p(k_{exp,p})$=$\frac{2\pi f_{exp,l,p}}{k_{exp,p}}$ is the velocity computed from the experimentally observed mode frequency at wave-vector $k_{exp,p}$.

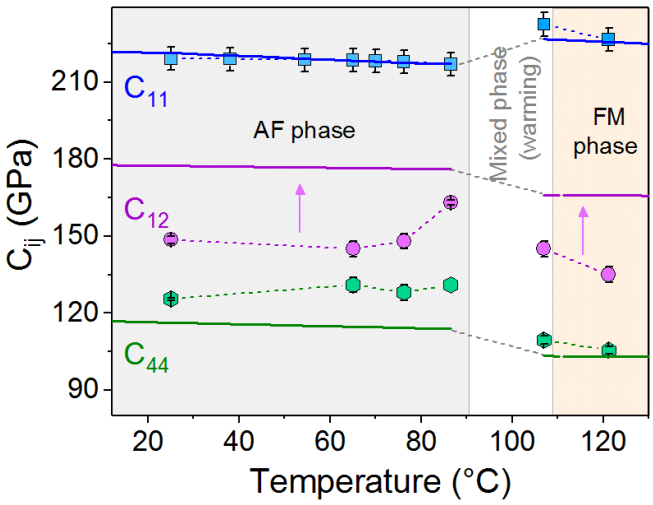

FIG. 5. Temperature-dependence of elastic constants of FeRh: determined by the analysis of the BLS and picosecond acoustics data (symbols with dashed lines, at more temperatures for the latter), or calculated by TDEP anharmonic lattice dynamics (full lines). Note that the latter were obtained in *both* phases in the entire temperature range, and that we are only showing values relevant to the experimentally observed phases.

Results

A typical adjustment in the AF phase at room-temperature is shown in Fig. 2(b), with the resulting calculated dispersion relation of the three acoustic modes plotted in full lines. An excellent agreement with the experimental data is found for the following FeRh constants: C_{11}=219, C_{12}=148 and C_{44}=125 GPa. Note that the calculated Sezawa modes only exist above a particular cut-off wave-vector (k_{S1}=1.58 and k_{S2}=10.25 μm^{-1}), a well-known feature of these semi-guided surface modes[27]. The fact that we nevertheless observe the guided modes below k_{S2} might be due to a slight misalignment off high-symmetry crystalline axis. We have discarded these points from the fitting procedure and only used points in the interval k=13-21.4 μm^{-1}. The fitting procedure is applied to all the temperatures of the warming branch of Fig. 3. The resulting temperature-dependent FeRh elastic constants are shown in Fig. 5, with the error bars reflecting the uncertainty on the film thickness (d=195±2 nm).

We find C_{44} has a rather flat behavior with temperature in the AF phase, and then decreases from 130 to 110 GPa at the transition. This drop is similar to the one seen by Cooke *et al.*, albeit on very different values (77 to 57 GPa) estimated quite indirectly from a heat capacity measurement. We evidence a non-monotonic evolution of C_{12} in the AF phase, with a sharp increase ($\approx$ 20 GPa) as the FM phase is approached. While this is not unheard of (C_{12}(T) of MgO is, for instance, non-monotonous at low temperatures [29]), one might wonder whether it is related to the volume increase taking place at the transition. There is no previous record of any estimate of C_{12} in either phase to compare our results to. Instead, we can "isotropize" our coefficients into a Young modulus E, using the well-known Hill method [30], and compare it to values of the literature. We find in the AF phase E_{AF}=187 GPa (T=86°C), and a higher value E_{FM}=198 GPa in the FM phase (T=107°C). This is reassuringly similar to the values found on polycristalline FeRh by both Palmer *et al.* [13]: E_{AF}=196 and E_{FM}=211 GPa ($T \approx$40°C), and by Ricodeau *et al.* [14, 31]: E_{AF}=170 ($T \approx$25°C) and E_{FM}=190 GPa ($T \approx$100°C). Let us recommend to compare absolute values of the elastic coefficients in different phases with caution if taken at very different temperatures, or Rh concentration, since both of these parameters have a strong influence. Comparing to other materials, it is worth mentionning that the elastic constants of FeRh (i) vary overall more weakly with temperature than for instance those of Fe [32] or MgO [29] (for which C_{11} loses ≈6 GPa, C_{12} ≈0.5 GPa and C_{44} ≈1-2 GPa between 25°C and 125°C), and (ii) are very similar, in the FM phase, to those of crystalline Iron taken at a similar temperature (T = 125°C [32]): C_{11}=225, C_{12}=133, C_{44}=114 GPa, to be compared to those we found for FeRh in the FM phase : C_{11}=227, C_{12}=145, C_{44}=109.5 GPa.

NUMERICAL ESTIMATES OF C_{ij} OF FeRh

We now discuss the first principles modelling of the elastic constants of FeRh. To compare quantitatively to our experiments, it is essential to go beyond the harmonic approximation, by including thermal expansion and intrinsic anharmonicity, in particular for AF FeRh. Existing T= 0 K theoreti-

cal studies in the literature predict the appearance of an imaginary phonon mode [17, 33–35], which prevents the evaluation of thermodynamic quantities.

We employ the temperature-dependent effective potential (TDEP) method [36–38] to include anharmonicity and renormalize phonon-phonon interactions. In order to reduce the simulation costs while keeping the accuracy of DFT, we constructed two machine-learning interatomic potential (MLIP [39]) models for the FM and AF phases. The details of the simulations are described in Appendix D. We calculate the elastic constants of both phases as a function of T (0 to 500 K, i.e -273 to 227°C) through their relation to the real space interatomic force constants. Aschauer *et al.* [17] in particular showed the importance of non-linear elasticity in FeRh. These effects on the measured C_{ij} are folded in through the temperature-dependence of the TDEP force constants.

Considering first T= 0 K DFT values, Table I shows that our results compare well with available literature [16, 17, 19], with slight differences that can be attributed to the choice of exchange and correlation functionals or the use of DFT+U. The temperature-dependence of the elastic constants of FeRh in both phases are then shown in Fig. 5, with values cut-off to mimic the experimentally observed warming transition.

When comparing to the experimentally determined values of C_{11}, C_{12} and C_{44}, a particularly good agreement is obtained for C_{11} in both phases, with a maximum discrepancy (in absolute value) of 2.4%. For the other C_{ij}s, the agreement is overall good, with a maximum discrepancy (in absolute value) of 23% for C_{12} and 13% for C_{44}. More importantly, the temperature evolution is well described, particularly the changes when going from the AF to the FM phase. It should be noted that explicitly including atomic vibrations in the temperature evolution is important for a quantitative description. In particular, and as shown in Appendix D, only including thermal expansion as a mechanism for the temperature evolution results in an overestimation of the C_{11} in the FM phase and the C_{44} in the AF phase.

Phase		C_{11} (GPa)	C_{12} (GPa)	C_{44} (GPa)
AF	**This work exp 25°C**	219	148	125
	This work DFT 25°C	224	177	116
	This work DFT 0K	239	184	129
	He *et al* DFT 0K [16]	219	188	120
	Aschauer *et al* DFT 0K [17]	225	181	120
FM	**This work exp 121°C**	227	145	109
	This work DFT 121°C	225	165	103
	This work DFT 0K	262	169	111
	He *et al* DFT 0K [16]	278	179	110
	Aschauer *et al* DFT 0K [17]	252	161	110
	Hao *et al* DFT 0K [19]	259	162	111

TABLE I. Survey of the elastic constants of the C_{ij} constants of FeRh obtained by DFT computations and this work, at 25°C in the AF phase and 121°C in the FM phase and comparison to our experimental data.

CONCLUSIONS

We measured the phonon dispersion relationship of epitaxial FeRh/MgO using Brillouin light scattering at variable temperature in both the uniform ferro- and anti-ferromagnetic phases of this material. Modeling the obtained dispersion by a "layer-on-substrate" approach, using the known parameters of MgO, and the independently measured C_{11} constant, we obtained the other two constants; C_{12}(T) and C_{44}(T). As is very often the case, C_{11} is substantially larger than the other two. Unlike the latter two, C_{11} is larger in the FM phase than in the AF phase. A temperature-dependent first principles modeling of the elastic constants renders the experimental values very closely. This work represents a substantial step towards the accurate modeling of the magnon-phonon interaction, thanks to a proper description of the elastic system in both phases, and at varying temperature. In this respect, it should also provide a new tool to determine the role of strain in the intriguing first-order AF-FM transition of FeRh.

APPENDIX A: DETAILS ON THE HEATING SYSTEM INTEGRATED IN THE BLS SETUP

In order to study the sample in both AF and FM phases, an in-situ heating system was integrated into the BLS bench. This system is placed in the air gap of an electromagnet consisting of a cylindrical oven with an internal diameter of 1 cm, having an electrical resistance of 380 Ω powered by a DC current source to ensure the heating. The sample is held on a metal rod with a thermal paste, inserted into the oven nearby a thermocouple probe to get the heating temperature which is adjusted from ambient to 150° C corresponding to a maximum current of 260 mA. For each temperature, the heating process, thermal equilibrium and spectrum acquisition take around 3 hours, corresponding on average to 1 count/minute for the Rayleigh peak.

APPENDIX B: PICOSECOND ACOUSTICS

The picosecond acoustic pump-probe set-up is described in Peronne *et al.* [26]. The Sagnac interferometer measures Im($\Delta r/r$) where r is the amplitude reflection coefficient of the light electric field. One can shows that this quantity gives the modification of the phase of the electric field of the light induced by the vertical displacement of the sample surface [40]. More specifically to these measurements, the laser repetition rate was 80 MHz, with a modulation of the pump at 1 MHz. Its wavelength was 773 nm, and the beam diameter was of the order of ≈ 15 µm. The power of the pump beam was around P=32 mW, that of the probe around 4 mW. The delay line was scanned mechanically at 40 nm/ps. In order to determine precisely the arrival time of the echoes, the thermal background is removed, and the peaks are fitted by a Lorentzian (inset of Fig. 4(a)).

APPENDIX C: DETAILS ON THE MODELING OF THE ACOUSTIC DISPERSION

In this appendix we give the cumbersome details on how the determinant of Eq. 1 is obtained. It is then used to determine the elastic constants of FeRh from the dispersion relation measured by BLS.

Waves and tensors are all given in the <100> reference frame of the cubic MgO substrate. For MgO we have:

$$[C_0]=\begin{pmatrix} C_{0,11} & C_{0,12} & C_{0,12} & 0 & 0 & 0 \\ C_{0,12} & C_{0,11} & C_{0,12} & 0 & 0 & 0 \\ C_{0,12} & C_{0,12} & C_{0,11} & 0 & 0 & 0 \\ 0 & 0 & 0 & C_{0,44} & 0 & 0 \\ 0 & 0 & 0 & 0 & C_{0,44} & 0 \\ 0 & 0 & 0 & 0 & 0 & C_{0,44} \end{pmatrix}$$

The elastic coefficient tensor of cubic FeRh has an identical symmetry, but needs to be $\pi/4$ rotated to render the epitaxial match condition of the layer on its substrate:

$$[C^*]=\begin{pmatrix} C^*_{11} & C^*_{12} & C^*_{13} & 0 & 0 & 0 \\ C^*_{12} & C^*_{11} & C^*_{12} & 0 & 0 & 0 \\ C^*_{13} & C^*_{12} & C^*_{33} & 0 & 0 & 0 \\ 0 & 0 & 0 & C^*_{44} & 0 & 0 \\ 0 & 0 & 0 & 0 & C^*_{44} & 0 \\ 0 & 0 & 0 & 0 & 0 & C^*_{66} \end{pmatrix}$$

with

$$\begin{cases} C^*_{11} &= \frac{1}{2}(C_{11}+C_{12})+C_{44} \\ C^*_{12} &= \frac{1}{2}(C_{11}+C_{12})-C_{44} \\ C^*_{13} &= C_{12} \\ C^*_{33} &= C_{11} \\ C^*_{44} &= C_{44} \\ C^*_{66} &= \frac{1}{2}(C_{11}-C_{12}) \end{cases}$$

Following Farnell *et al.* [27], the procedure to obtain the dispersion relationship of the FeRh/MgO system is the following: (i) fix a wavevector k, (ii) calculate the implicit relationship relating the Rayleigh wave velocity V to the elastic constants of each material, (iii) find the solution $V(k)$ satisfying the boundary conditions at the film/substrate and air/film interfaces.

With z the normal to the film and x||[100], the partial waves propagating in MgO and FeRh along x are respectively of the form:

$$u_0(x,z,t) = \sum_{i=1,2} \begin{pmatrix} U_{x,0i} \\ 0 \\ U_{z,0i} \end{pmatrix} e^{-q_{0,i}kz}.e^{j(\omega t-kx)} \quad (3)$$

$$u(x,z,t) = \sum_{i=1-4} \begin{pmatrix} U_{x,i} \\ 0 \\ U_{z,i} \end{pmatrix} e^{-q_{i}kz}.e^{j(\omega t-kx)} \quad (4)$$

The dimensionless coefficients $q_{0,i}, q_i$ convey the penetration profile of the displacements u, u_0. Injecting these waveforms into the elastic equation of motion leads to the two quadratic equations 5, 6. We label $q_{i,0}$ (i=1,2) the two roots of Eq. 5 exhibiting a positive real part, and q_i (i=1-4) the four roots of Eq. 6. ρ_0 and ρ are the volume densities of MgO and FeRh respectively.

$$q_0^4+\left(\frac{-C_{0,44}^2-C_{0,11}^2+(C_{0,12}+C_{0,44})^2+\rho_0V^2(C_{0,11}+C_{0,44})}{C_{0,11}C_{0,44}}\right)q_0^2+\frac{(\rho_0V^2-C_{0,11})(\rho_0V^2-C_{0,44})}{C_{0,11}C_{0,44}} = 0 \quad (5)$$

$$q^4+\left(\frac{-C_{44}^{*2}-C^*_{11}C^*_{33}+(C^*_{13}+C^*_{44})^2+\rho V^2(C^*_{33}+C^*_{44})}{C^*_{33}C^*_{44}}\right)q^2+\frac{(\rho V^2-C^*_{11})(\rho V^2-C^*_{44})}{C^*_{33}C^*_{44}} = 0 \quad (6)$$

The ratio of the amplitudes of the out-of-plane and in-plane displacements for each solution in MgO and FeRh are labelled $r_{0,i}$ and r_i. They are given by Eqs. 7, 8, in which we recall that the $q_{0,i}, q_i$ depend on V.

$$r_{0,i}(V,k) = \frac{U_{z,0i}}{U_{x,0i}} = \frac{C_{11,0}-q_{0,i}^2C_{44,0}-\rho_0V^2}{jq_{0,i}(C_{12,0}+C_{44,0})} \quad (7)$$

$$r_i(V,k) = \frac{U_{z,i}}{U_{x,i}} = \frac{C^*_{11}-q_i^2C^*_{44}-\rho V^2}{jq_i(C^*_{13}+C^*_{44})} \quad (8)$$

Finally, the conditions of continuous displacements and tangential and normal stresses across the interface, and zero stress at the surface leads to a system of 6 equations with six unknown amplitudes $(U_{x,01}, U_{x,02}, U_{x,1}, U_{x,2}, U_{x,3}, U_{x,4})$. In order to find the velocity V corresponding to the chosen k, one must thus find the roots V_i of the 6×6 determinant $\mathscr{D}(V)$ given in the main text, Eq. 1. The velocity intervenes through the dependency $q_{0,i}(V,k), q_i(V,k)$ and $r_{0,i}(V,k), r_i(V,k)$ in the coefficients $a_{0,i}, a_i$ and $b_{0,i}, b_i$:

$$a_{0,i}(V,k) = \frac{C_{44,0}}{C_{44}}(q_{0,i} + jr_{0,i}) \quad (9)$$

$$a_i(V,k) = q_i + jr_i \quad (10)$$

$$b_{0,i}(V,k) = jC_{12,0} + C_{11,0}q_{0,i}r_{0,i} \quad (11)$$

$$b_i(V,k) = jC^*_{13} + C^*_{33}q_i r_i \quad (12)$$

The numerical values for $C_{0,ij}(T)$ and $\rho_0(T)$ of MgO were taken from Sumino *et al.* [29]. The volume density of FeRh was taken phase-dependent with ρ_{FM}=ρ_{AF}/1.07=9957.7 kg m^{-3}, where ρ_{AF}=9888.49 kg m^{-3} was computed from in-plane and out-of-plane lattice parameters $a_{||,AF}$ = 2.987 Å and $c_{\perp,AF}$ = 2.988 Å measured by X-ray diffraction at room temperature [9, 24].

APPENDIX D: DETAILS ON THE FIRST PRINCIPLES ANHARMONIC MODELING

First principles forces and Machine-learning interatomic potential

As a reference potential for the MLIP, we performed DFT calculations with the Abinit suite [41, 42], using the PBE [43] parametrization of the exchange and correlation functional in the PAW formalism [44, 45]. To ensure the convergence of the calculations, the kinetic energy cutoff was set to 20 Ha, while the Brillouin zone integration was discretized on a $21 \times 21 \times 21$ k-point grid. The ground state lattice constants obtained with these parameters are shown in Table II. They are in agreement with previous theoretical results [17, 35] and very close to room-temperature experimental values [24].

The MLIP were constructed using the Moment Tensor Potential [39, 46]. For both phases, we set the level of the MLIP to 22 and a cutoff of 5.6 is used, in order to ensure an accurate description of important interactions for the B2 structure [47]. In the AF phase, to account for the spin-dependent interactions between atoms, the spin up and down Fe atoms were considered as distinct elements in the descriptor. The DFT dataset was constructed self-consistently following the MLACS algorithm [48], in which a molecular dynamics trajectory is driven by a MLIP which is trained regularly on configurations extracted from this dynamics. It should be noted that the configurations are chosen randomly and not based on an extrapolation criterion [49], to improve on the measure defined in [48]. After each new addition to the database, the thermostat and barostat of the MD run were set to randomly generated temperature and pressure in the range 20 to 1200 K and -2 to 2 GPa, to ensure a stable MLIP in the range of thermodynamic conditions considered in this work. To improve the description of elastic properties, some strained configurations were also included in the dataset. Once enough data is available, the potential is validated by splitting the dataset into testing and training sets, and the final MLIP were fit using the energy, forces and stress.

The resulting MLIP provides an accurate representation of the potential energy surface provided by the DFT, as shown in the good agreement for structural properties in Table II and the energy, forces and stress correlation shown in Fig. 6.

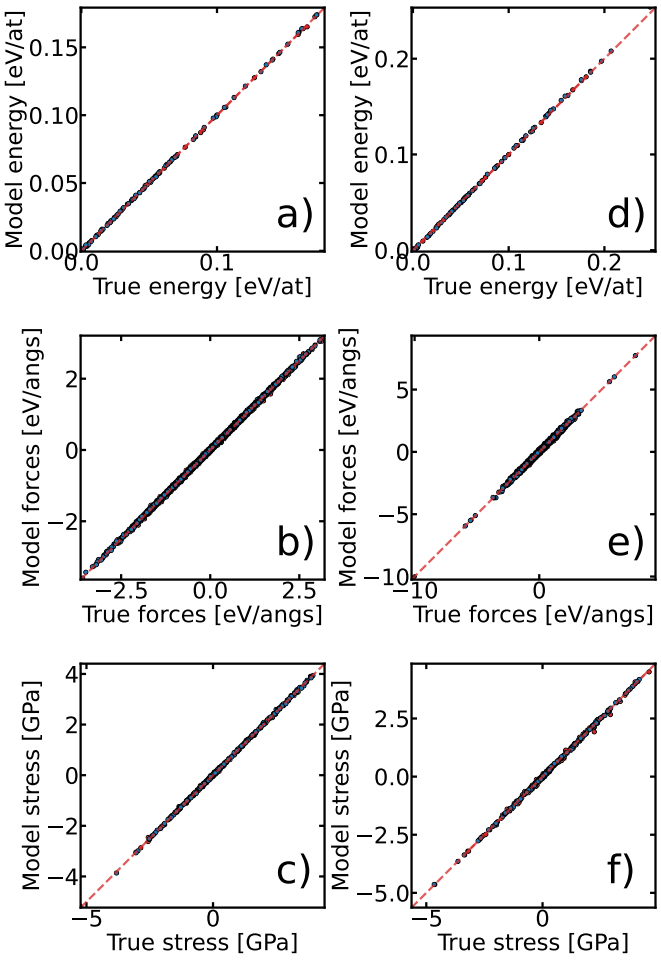

FIG. 6. Correlation plot between the MLIP and the DFT datasets. Plot a), b) and c) are for the AF phase, and d), e) and f) are for the FM phase.

	a (Å)	C_{11} (GPa)	C_{12} (GPa)	C_{44} (GPa)
DFT AF	3.004	231	188	121
MLIP AF	3.004	239	184	129
DFT FM	3.019	267	169	114
MLIP FM	3.020	262	169	111

TABLE II. Comparison of structural properties at 0 K computed with DFT and the MLIP using finite deformation and fitted using the elastic package [50].

Molecular dynamics

With the MLIP, we compute the effective anharmonic Hamiltonian from 50 to 450 K in steps of 50 K. For each temperature, we run two 100 ps MD simulations on $8 \times 8 \times 8$ supercells, with a time step of 1 fs using the LAMMPS package [51]. The first MD run is performed in the NPT (isothermal-isobaric) ensemble, and is used to compute the average equilibrium volume, while the second one employs this equilibrium volume in the NVT (canonical) ensemble. Post-processing is done using 900 uncorrelated configurations, extracted from the MD trajectory after 25 ps of equilibration.

Temperature-dependent elastic constants

To describe the influence of the temperature on the elastic constants, a common approximation is to neglect the explicit effects of atomic vibrations and consider that the C_{ij} evolve only through the thermal expansion as

$$C_{\alpha\beta\gamma\delta}(\Omega,T) = C_{\alpha\beta\gamma\delta}(\Omega(T),0) \tag{13}$$

where $\Omega(T)$ is the volume. While this method often brings a good description of the temperature evolution of the elastic constants, explicit effects of the temperature can be important to be quantitative.

To go beyond this approximation, we can use the fact that elastic constants are related to long wavelength phonons and can be extracted using the slope of the acoustic dispersion close to the Γ point. Then, introducing the temperature evolution of the phonons to extract the slope allows to include the effects of temperature on the elastic properties. The slope of the acoustic dispersion can be directly extracted from the interatomic force constants $\mathbf{\Phi}$ as[52, 53]

$$C_{\alpha\beta\gamma\delta}(\Omega,T) = -\frac{1}{2\Omega}\sum_{ij}\Phi_{ij}^{\alpha\beta}(\Omega,T)d_{ij}^{\gamma}d_{ij}^{\delta} \tag{14}$$

where d_{ij}^{γ} is the distance between the unitcells of atom i and j along Cartesian direction γ.

To introduce finite temperature renormalization of the interatomic force constant, and consequently of the $C_{\alpha\beta\gamma\delta}$ tensor, we use the Temperature-Dependent Effective Potential (TDEP) method. The method works by performing a least-squares fit of the $\mathbf{\Phi}(\Omega,T)$ tensor using a set of forces and displacements extracted from a NVT molecular dynamics run [36, 37]. We used the implementation provided by the TDEP package [54].

We compare the temperature dependence of both approaches in Fig. 7. While most of the C_{ij} changed very little when introducing atomic vibrations in the description, the FM C_{11} and the AF C_{44} are significantly reduced.

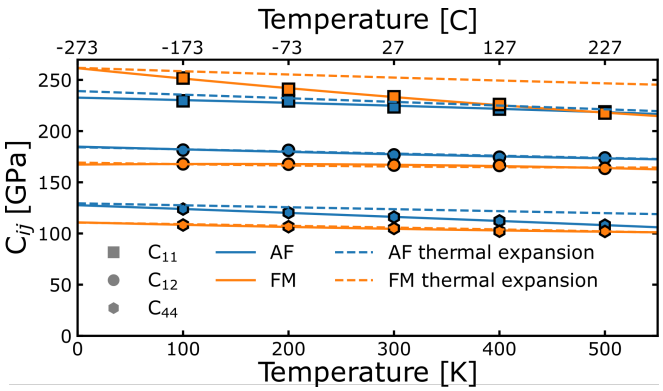

FIG. 7. Theoretical prediction of C_{ij}s of FeRh in the FM and AF phases. Markers are the direct prediction of the elastic constants using the TDEP method and full lines are a 3rd order polynomial fit. Dashed lines present results when only considering thermal expansion in the temperature evolution of the elastic constants.

ACKNOWLEDGMENTS

This work has been partly supported by the French Agence Nationale de la Recherche (ANR ACAF 20-CE30-0027). Access to the CEITEC Nano Research Infrastructure was supported by the Ministry of Education, Youth and Sports (MEYS) of the Czech Republic under the project Czech-NanoLab (LM2023051). AC and MJV acknowledge the Fonds de la Recherche Scientifique (FRS-FNRS Belgium) for PdR Grant No. T.0103.19 - ALPS, and ARC project DREAMS (G.A. 21/25-11) funded by Federation Wallonie Bruxelles and ULiege. Simulation time was awarded by the Belgian share of EuroHPC in LUMI hosted by CSC in Finland, by the CECI (FRS-FNRS Belgium Grant No. 2.5020.11), as well as the Zenobe Tier-1 of the Fédération Wallonie-Bruxelles (Walloon Region grant agreement No. 1117545).

We acknowledge the technical assistance of Mathieu Bernard from Institut des Nanosciences de Paris.

[1] M. Fallot, Annales de physique **11**, 291 (1938).
[2] T. Moriyama, N. Matsuzaki, K.-J. Kim, I. Suzuki, T. Taniyama, and T. Ono, Applied Physics Letters **107**, 122403 (2015).
[3] X. Marti, I. Fina, C. Frontera, J. Liu, P. Wadley, Q. He, R. J. Paull, J. D. Clarkson, J. Kudrnovský, I. Turek, J. Kuneš, D. Yi, J.-H. Chu, C. T. Nelson, L. You, E. Arenholz, S. Salahuddin, J. Fontcuberta, T. Jungwirth, and R. Ramesh, Nature Materials **13**, 367 (2014), arXiv:0402594v3 [arXiv:cond-mat].
[4] H. Wu, H. Zhang, B. Wang, F. Groß, C. Y. Yang, G. Li, C. Guo, H. He, K. Wong, D. Wu, X. Han, C. H. Lai, J. Gräfe, R. Cheng, and K. L. Wang, Nature Communications **13**, 1 (2022).
[5] N. A. Blumenschein, G. M. Stephen, C. D. Cress, S. W. LaGasse, A. T. Hanbicki, S. P. Bennett, and A. L. Friedman, Scientific Reports **12**, 22061 (2022).
[6] Y. Liu, L. C. Phillips, R. Mattana, M. Bibes, A. Barthélémy, and B. Dkhil, Nature Communications **7**, 11614 (2016).

[7] J. Lyubina, Journal of Physics D: Applied Physics **50**, 053002 (2017).

[8] V. Uhlíř, J. A. Arregi, and E. E. Fullerton, Nature Communications **7**, 13113 (2016), arXiv:1605.06823.

[9] J. A. Arregi, O. Caha, and V. Uhlíř, Physical Review B **101**, 174413 (2020).

[10] F. Pressacco, D. Sangalli, V. Uhlíř, D. Kutnyakhov, J. A. Arregi, S. Y. Agustsson, G. Brenner, H. Redlin, M. Heber, D. Vasilyev, J. Demsar, G. Schönhense, M. Gatti, A. Marini, W. Wurth, and F. Sirotti, Nature Communications **12**, 5088 (2021), arXiv:2102.09265.

[11] S. O. Mariager, F. Pressacco, G. Ingold, A. Caviezel, E. Möhr-Vorobeva, P. Beaud, S. L. Johnson, C. J. Milne, E. Mancini, S. Moyerman, E. E. Fullerton, R. Feidenhans'l, C. H. Back, and C. Quitmann, Physical Review Letters **108**, 087201 (2012).

[12] D. W. Cooke, F. Hellman, C. Baldasseroni, C. Bordel, S. Moyerman, and E. E. Fullerton, Physical Review Letters **109**, 255901 (2012).

[13] S. B. Palmer, P. Dentschuk, and D. Melville, Physica Status Solidi (a) **32**, 503 (1975).

[14] J. A. Ricodeau and D. Melville, Journal of Physics F: Metal Physics **2**, 337 (1972).

[15] A. Castets, D. Tochetti, and B. Hennion, Physica B+C **86-88**, 353 (1977).

[16] W. He, H. Huang, and X. Ma, Materials Letters **195**, 156 (2017).

[17] U. Aschauer, R. Braddell, S. A. Brechbühl, P. M. Derlet, and N. A. Spaldin, Physical Review B **94**, 014109 (2016), arXiv:1603.01827.

[18] M. J. Jiménez, A. B. Schvval, and G. F. Cabeza, Computational Materials Science **172**, 109385 (2020).

[19] Y. Hao, L. Zhang, and J. Zhu, Zeitschrift für Naturforschung A **75**, 789 (2020).

[20] J. Gump, H. Xia, M. Chirita, R. Sooryakumar, M. A. Tomaz, and G. R. Harp, Journal of Applied Physics **86**, 6005 (1999).

[21] G. Carlotti, J. Sadhu, and F. Dumont, in *2017 IEEE International Ultrasonics Symposium (IUS)* (IEEE, 2017) pp. 1–1.

[22] J. O. Kim, J. D. Achenbach, P. B. Mirkarimi, M. Shinn, and S. A. Barnett, Journal of Applied Physics **72**, 1805 (1992).

[23] P. Hemme, P. Djemia, P. Rovillain, Y. Gallais, A. Sacuto, A. Forget, D. Colson, E. Charron, B. Perrin, L. Belliard, and M. Cazayous, Applied Physics Letters **118** (2021), 10.1063/5.0039505.

[24] J. A. Arregi, F. Ringe, J. Hajduček, O. Gomonay, T. Molnár, J. Jaskowiec, and V. Uhlíř, Journal of Physics: Materials **6**, 034003 (2023).

[25] S. Maat, J.-U. Thiele, and E. E. Fullerton, Physical Review B **72**, 214432 (2005).

[26] E. Péronne, N. Chuecos, L. Thevenard, and B. Perrin, Physical Review B **95**, 064306 (2017).

[27] W. G. W. Farnell, in *Topics in Applied Physics* (Berlin, Heidelberg, 1978) springer ed., pp. 13–60.

[28] Y. Bar-Cohen and A. K. Mal, Journal of the Acoustical Society of America **88**, 482 (1990).

[29] Y. Sumino, O. L. Anderson, and I. Suzuki, Physics and Chemistry of Minerals **9**, 38 (1983).

[30] R. Hill, Proceedings of the Physical Society. Section A **65**, 349 (1952).

[31] A. I. Zakharov, A. M. Kadomtseva, R. . Z. Levitin, and E. G. Ponyatovskil, J. Exptl. Theoret. Phys. (U.S.S.R.) **19** (1964).

[32] J. J. Adams, D. S. Agosta, R. G. Leisure, and H. Ledbetter, Journal of Applied Physics **100** (2006), 10.1063/1.2365714.

[33] J. Kim, R. Ramesh, and N. Kioussis, Physical Review B **94**, 180407(R) (2016).

[34] N. A. Zarkevich and D. D. Johnson, Physical Review B **97**, 014202 (2018), arXiv:1710.04199.

[35] M. P. Belov, A. B. Syzdykova, and I. A. Abrikosov, Physical Review B **101**, 134303 (2020).

[36] O. Hellman, I. A. Abrikosov, and S. I. Simak, Physical Review B **84**, 180301 (2011).

[37] O. Hellman and I. A. Abrikosov, Physical Review B **88**, 144301 (2013).

[38] O. Hellman and D. A. Broido, Physical Review B **90**, 134309 (2014).

[39] A. V. Shapeev, Multiscale Modeling and Simulation **14**, 1153–1173 (2016).

[40] C. Thomsen, H. Grahn, H. Maris, and J. Tauc, Physical Review B **34**, 4129 (1986).

[41] X. Gonze, B. Amadon, G. Antonius, F. Arnardi, L. Baguet, J.-M. Beuken, J. Bieder, F. Bottin, J. Bouchet, E. Bousquet, N. Brouwer, F. Bruneval, G. Brunin, T. Cavignac, J.-B. Charraud, W. Chen, M. Côté, S. Cottenier, J. Denier, G. Geneste, P. Ghosez, M. Giantomassi, Y. Gillet, O. Gingras, D. R. Hamann, G. Hautier, X. He, N. Helbig, N. Holzwarth, Y. Jia, F. Jollet, W. Lafargue-Dit-Hauret, K. Lejaeghere, M. A. Marques, A. Martin, C. Martins, H. P. Miranda, F. Naccarato, K. Persson, G. Petretto, V. Planes, Y. Pouillon, S. Prokhorenko, F. Ricci, G.-M. Rignanese, A. H. Romero, M. M. Schmitt, M. Torrent, M. J. van Setten, B. V. Troeye, M. J. Verstraete, G. Zérah, and J. W. Zwanziger, Computer Physics Communications **248**, 107042 (2020).

[42] A. H. Romero, D. C. Allan, B. Amadon, G. Antonius, T. Applencourt, L. Baguet, J. Bieder, F. Bottin, J. Bouchet, E. Bousquet, F. Bruneval, G. Brunin, D. Caliste, M. Côté, J. Denier, C. Dreyer, P. Ghosez, M. Giantomassi, Y. Gillet, O. Gingras, D. R. Hamann, G. Hautier, F. Jollet, G. Jomard, A. Martin, H. P. C. Miranda, F. Naccarato, G. Petretto, N. A. Pike, V. Planes, S. Prokhorenko, T. Rangel, F. Ricci, G.-M. Rignanese, M. Royo, M. Stengel, M. Torrent, M. J. van Setten, B. V. Troeye, M. J. Verstraete, J. Wiktor, J. W. Zwanziger, and X. Gonze, J. Chem. Phys. **152**, 124102 (2020).

[43] J. P. Perdew, K. Burke, and M. Ernzerhof, Physical Review Letters **77**, 3865 (1996).

[44] P. E. Blöchl, Physical Review B **50**, 17953 (1994).

[45] F. Jollet, M. Torrent, and N. Holzwarth, Computer Physics Communications **185**, 1246 (2014).

[46] I. S. Novikov, K. Gubaev, E. V. Podryabinkin, and A. V. Shapeev, Machine Learning: Science and Technology **2**, 025002 (2021).

[47] S. Ono and D. Kobayashi, Scientific Reports **12** (2022), 10.1038/s41598-022-10658-2.

[48] A. Castellano, F. m. c. Bottin, J. Bouchet, A. Levitt, and G. Stoltz, Physical Review B **106**, L161110 (2022).

[49] E. V. Podryabinkin and A. V. Shapeev, Computational Materials Science **140**, 171–180 (2017).

[50] Paweł T. Jochym and Codacy Badger, "jochym/elastic: Maintenance release," (2018).

[51] A. P. Thompson, H. M. Aktulga, R. Berger, D. S. Bolintineanu, W. M. Brown, P. S. Crozier, P. J. in 't Veld, A. Kohlmeyer, S. G. Moore, T. D. Nguyen, R. Shan, M. J. Stevens, J. Tranchida, C. Trott, and S. J. Plimpton, Computer Physics Communications **271**, 108171 (2022).

[52] in *Statistical Physics of Crystals and Liquids* (WORLD SCIENTIFIC, 2003) p. 115–153.

[53] G. Leibfried and W. Ludwig, "Theory of anharmonic effects in crystals," in *Solid State Physics* (Elsevier, 1961) p. 275–444.

[54] F. Knoop, N. Shulumba, A. Castellano, J. P. A. Batista, R. Farris, M. J. Verstraete, M. Heine, D. Broido, D. S. Kim, J. Klar-

726 bring, I. A. Abrikosov, S. I. Simak, and O. Hellman, Journal of 727 Open Source Software **9**, 6150 (2024).